Coupled dynamics of the North Equatorial Countercurrent and Intertropical Convergence Zone with relevance to the double-ITCZ problem

Zhiyuan Li, Alexey Fedorov

PNAS RESEARCH ARTICLE | EARTH, ATMOSPHERIC, AND PLANETARY SCIENCES

Coupled dynamics of the North Equatorial Countercurrent and Intertropical Convergence Zone with relevance to the double-ITCZ problem

Zhiyuan Li[a,1] and Alexey V. Fedorov[a,b]

Edited by Kerry Emanuel, Massachusetts Institute of Technology, Cambridge, MA; received November 10, 2021; accepted June 2, 2022

The Intertropical Convergence Zone (ITCZ) is a salient feature of tropical atmospheric circulation characterized by intense convective clouds and rainfall north of the equator. Climate models, however, commonly experience the double-ITCZ problem—the tendency to produce another strong precipitation band but south of the equator. Here, we describe coupled interaction between the ITCZ and the North Equatorial Countercurrent (NECC) that is relevant to this problem. This current is a major component of the tropical Pacific upper-ocean circulation, which flows against easterly trade winds and transports warm water from the western Pacific eastward. Its core follows the latitudinal position of the ITCZ. Trade winds converge toward the ITCZ, creating a local minimum in zonal winds and generating positive wind stress curl that maintains an eastward current despite westward winds. We show that interaction between the ITCZ and the NECC involves positive feedback: a stronger NECC advects warm water from the western Pacific to the colder east thus increasing sea surface temperature (SST) along its path, intensifying convection within the ITCZ and hence strengthening wind stress curl, further strengthening the NECC. To demonstrate this wind stress curl-advection-SST-precipitation (WASP) feedback, we conduct climate model experiments in which we progressively strengthen the surface Ekman component of the NECC and observe the intensification of the ITCZ and the entire NECC. Consequently, a weak NECC leads to a weak ITCZ, which can contribute to the double-ITCZ problem in climate models, since weak wind convergence north of the equator enables stronger convergence in the south.

double-ITCZ bias | WASP feedback | NECC-ITCZ interaction | model simulation

Significance

In this paper, we investigate coupled interaction between the North Equatorial Countercurrent (NECC) and the Intertropical Convergence Zone (ITCZ)—two fundamental features of the tropical oceanic and atmospheric circulations, respectively. We show that this interaction involves positive feedback that connects several crucial dynamical variables including wind stress curl, zonal advection, sea surface temperature and precipitation. By underestimating this feedback, climate models produce a too-weak NECC, which contributes to the models' tendency to generate another strong precipitation band but south of the equator (model bias known as the double-ITCZ problem). The role of the coupling between the NECC and ITCZ and its relevance for the double-ITCZ problem are highlighted in a suite of numerical experiments.

One of the most striking features of ocean circulation in the tropical Pacific is the North Equatorial Countercurrent (NECC)—a swift, nearly zonal upper-ocean current flowing across the North Pacific from west to east against the predominantly easterly trade winds (Fig. 1; 1–6). This current is positioned between roughly 4°N and 10°N and flows in a narrow band between two westward currents, the northern branch of the South Equatorial Current (SEC) and the North Equatorial Current (NEC). The spatial structure and intensity of the NECC varies seasonally and responds to changes in equatorial winds with stronger transport in the Summer-Fall season (2, 3, 7). It is centered at ∼5°N in the western tropical Pacific but shifts slightly poleward as it flows eastward to approximately 7–8°N in the central and eastern Pacific (4, 8). The current's maximum velocity reaches nearly 0.5 m/s (8). The NECC does not typically penetrate deeper than 200–300 m, and flows mainly above the thermocline (6, 8). A similar countercurrent exists in the Atlantic as well (9).

The location of the core of NECC generally coincides with the latitudinal position of the Intertropical convergence zone (ITCZ)—a fundamental feature of the tropical atmosphere characterized by atmospheric deep convection, intense precipitation and enhanced cloudiness (11). The southeast trade winds from the Southern Hemisphere and the northeast trade winds from the Northern Hemisphere converge along the ITCZ, which leads to vanishing meridional velocity and a local minimum in zonal winds and wind stress (12). A schematic diagram connecting the ITCZ, wind forcing, and tropical ocean currents is shown in Fig. 1*B*. The local zonal wind stress minimum is critical for the existence of the NECC as discussed below.

The winds deform sea surface height (SSH) via divergence or convergence of Ekman transport (green arrows in Fig. 1*B*). Specifically, negative wind stress curl leads to Ekman transport convergence, resulting in higher SSH and Ekman pumping (downwelling). Positive wind stress curl leads to Ekman transport divergence, a negative SSH anomaly and Ekman suction (upwelling). Therefore, increasingly strong trade winds north of the local zonal wind minimum near 7°N produce divergent Ekman transport

Author affiliations: [a]Department of Earth and Planetary Sciences, Yale University, New Haven, CT 06520; and [b]LOCEAN/IPSL, Sorbonne University, 75252 Paris, France

Author contributions: Z.L. and A.V.F. designed research; Z.L. performed research; Z.L. contributed new reagents/analytic tools; Z.L. analyzed data; and Z.L. and A.V.F. wrote the paper.

The authors declare no competing interest.

This article is a PNAS Direct Submission.

[1]To whom correspondence may be addressed. Email: zhiyuan.li@yale.edu.

This article contains supporting information online at http://www.pnas.org/lookup/suppl/doi:10.1073/pnas.2120309119/-/DCSupplemental.

Published July 26, 2022.

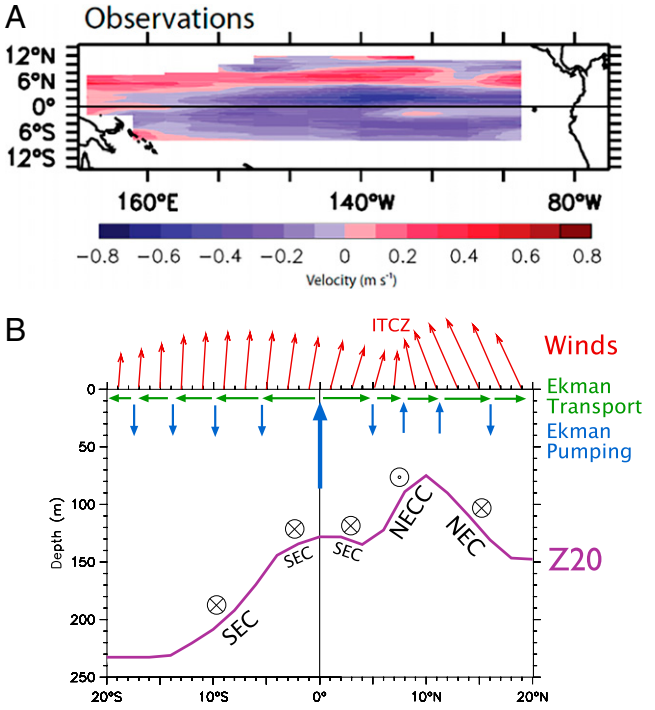

Fig. 1. (*A*) Observations and (*B*) a schematic for the upper-ocean zonal currents in the tropical Pacific. Red arrows represent surface winds. Green arrows indicate meridional Ekman transport induced by the zonal wind component. Vertical blue arrows show Ekman pumping (downwelling) and Ekman suction (upwelling) associated with Ekman transport convergence and divergence, respectively. The purple curve (Z20) refers to the depth of the 20 °C isotherm (a proxy for the thermocline depth). The directions of the NEC and SEC (both westward) and the NECC (eastward) are also shown. (*A*) From Brown and Fedorov (2008) (10) and is based on data from Johnson et al. (2002) (8). The schematic in (*B*) is courtesy of Billy Kessler.

(Fig. 1*B*), upwelling the thermocline and lowering SSH to the north thus creating a northward pressure gradient force. This wind pattern is zonally oriented across most of the basin, producing corresponding zonal thermocline ridges and troughs. The meridional slopes on their flanks set the zonal geostrophic currents which flow along ridge-trough contours, balancing the Coriolis force by turning to the right of the pressure gradient vector in the northern hemisphere. Consequently, the geostrophic NECC flows east along the slope between the thermocline trough near 3°N and the ridge near 10°N (Fig. 1*B*). At the same time, an integral of vorticity-based Sverdrup transport (*Materials and Methods*) explains the westward increase of NECC transport in both observations (Fig. 1*A*) and numerical models (Fig. 2 *B* and *C*).

A number of studies have focused on the response of the NECC to migrating zonal winds (2) arising in the context of the ITCZ latitudinal migration associated with the seasonal and ENSO cycles. However, little work has been done on how the ITCZ would respond to changes in the NECC, even though eastward advection of warm waters by the NECC has been previously suggested to contribute to the asymmetry of the ITCZ with respect to the equator (13, 14).

The potential effect of the NECC on the ITCZ makes their coupled interaction relevant to the climate models' tendency to generate two, sometimes nearly symmetric annual mean precipitation bands (north and south of the equator). This common problem, known as the double-ITCZ problem, represents the most significant model bias in tropical precipitation (15–18). A too-weak NECC would result in a weak ITCZ, which in turn may lead to the strengthening of the convergence zone south of the equator (19).

Accordingly, the goal of the present study is to investigate systematically the coupled dynamics of the NECC and the ITCZ using sensitivity experiments within a fully coupled climate model. Ultimately, this study shows that the NECC and ITCZ are linked via positive feedback that we refer to as the wind stress curl-advection-sea surface temperature (SST)-precipitation (WASP) feedback: a stronger NECC transports warmer water from the western Pacific warm pool to the central and eastern Pacific thus increasing SST along the NECC path, intensifying convection within the ITCZ and hence strengthening wind convergence and wind stress curl, further strengthening the NECC. To demonstrate the importance of the WASP feedback and investigate the ITCZ/NECC two-way coupling, we conduct coupled model experiments perturbing the NECC by modifying vertical eddy viscosity along the NECC path thus changing the Ekman component of the flow. We then assess the impacts of the imposed changes on the climate system.

Results

Conceptually, near the ocean surface the NECC can be decomposed into eastward geostrophic and westward Ekman components (*Materials and Methods*). The latter component is maintained by easterly trade winds dominant in the tropical Pacific (*SI Appendix*, Fig. S1*A*). The surface Ekman velocity is inversely proportional to the square root of vertical eddy viscosity ($u_{Ek} = \tau/\rho\sqrt{2\nu f}$; *Materials and Methods*). Therefore, for instance, reducing viscosity would strengthen the surface Ekman flow, thus reducing the NECC total surface velocity. *SI Appendix*, Fig. S1 *B* and *C* demonstrates this effect and shows estimated anomalies in the surface zonal Ekman velocity, if one changes vertical viscosity by factors

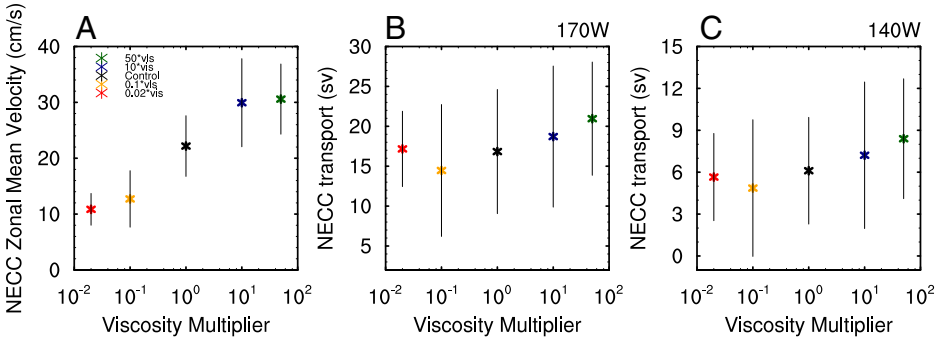

Fig. 2. (*A*) Maximum zonal mean velocity of the simulated NECC. (*B* and *C*) NECC total volume transport at 170°W and 140°W, respectively, as a function of the VM that we use to increase or decrease the vertical viscosity coefficient computed by the model within the band 4N°–10°N, 130°E–90°W, and 0–100 m in the perturbation experiments. The control experiment corresponds to VM = 10° = 1. See *Materials and Methods* for how the NECC maximum zonal mean velocity in (*A*) is defined.

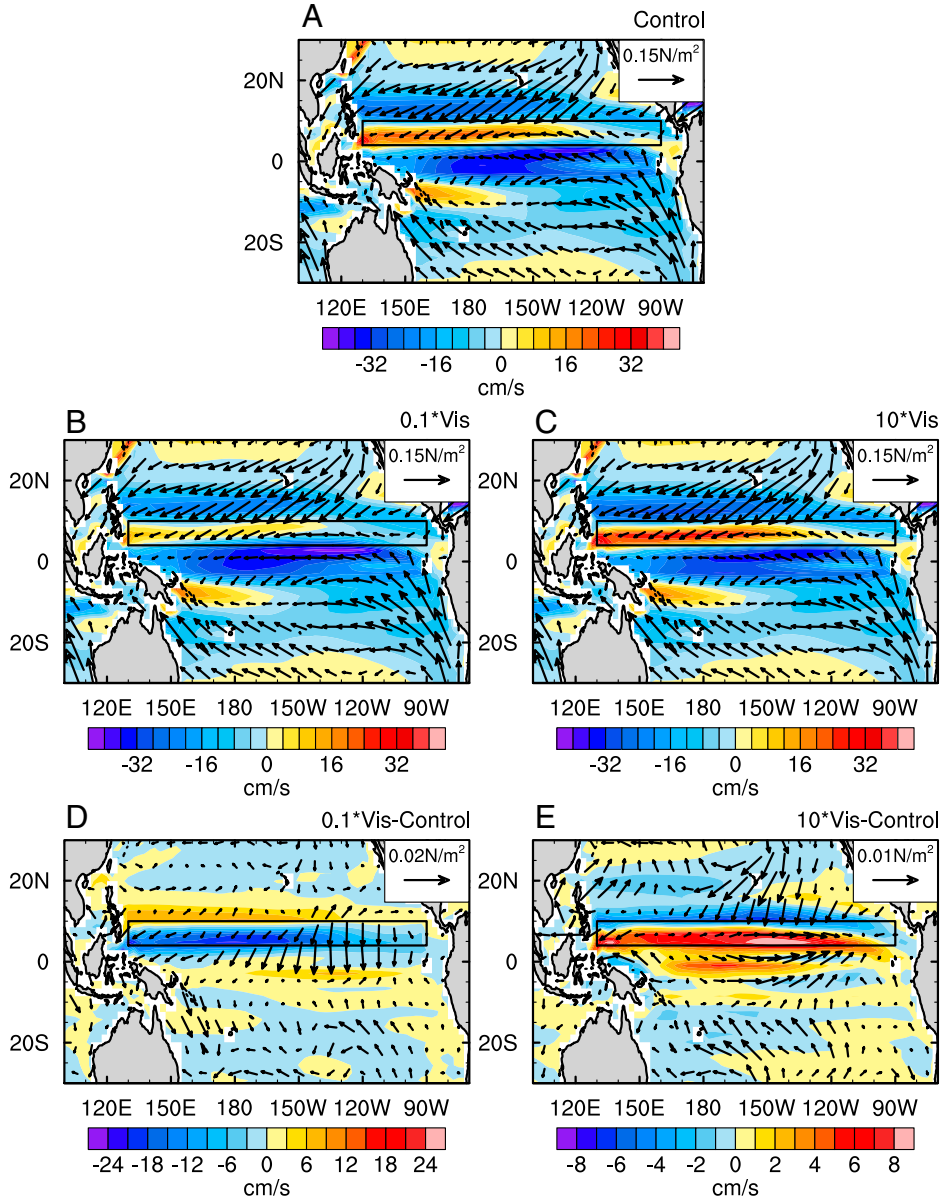

Fig. 3. (*A–C*) Ocean annual mean surface zonal velocity (colors) and wind stress (vectors) in the control simulation and the 0.1*Vis and 10*Vis experiments. Anomalies in the perturbation experiments relative to the control are shown in (*D*) and (*E*). The model vertical viscosity is modified inside the black box, which spans 4°N–10°N, 130°E–90°W, and 0–100 m. Unlike the results in *SI Appendix*, Fig. S1, here the coupled system is allowed to adjust to the imposed viscosity modifications, leading to further changes in the velocity field, wind stress, and other variables.

of 0.1 and 10, respectively, without any further adjustment in the system. These anomalies are based on the wind stress from the control run and thus represent the immediate effect of viscosity change on Ekman velocity unaffected by ocean-atmosphere coupling.

We conduct a suite of perturbation experiments, in which we vary eddy viscosity along the NECC path in a broad range (*Materials and Methods*). We refer to these experiments as 50*Vis, 10*Vis, 0.1*Vis, and 0.02*Vis, where "Vis" indicates the vertical viscosity coefficient that the model computes from a standard mixing parameterization, and the multiplier in front is used to increase or decrease viscosity in a particular experiment. We note, however, that the resultant viscosity that the model uses (i.e., output viscosity) varies in a much smaller range than the viscosity multipliers would suggest (*Materials and Methods* and *SI Appendix*, Fig. S7).

We find that the NECC maximum zonal mean velocity increases monotonically when vertical viscosity is increased (Fig. 2). Similarly, the total volume transport of the NECC increases monotonically as a function of viscosity, except for the 0.02*Vis experiment (Fig. 2 *B* and *C*). This experiment has low viscosity such that the Ekman layer depth becomes comparable with the vertical resolution of the model, which may have contributed to this result. Changes in the total volume transport throughout these experiments confirm the importance of ocean-atmosphere coupling in the perturbation experiments since wind changes are necessary to alter the volume transport.

Next, we consider how the induced initial changes in the surface Ekman flow would affect the entire NECC-ITCZ system via ocean-atmosphere interactions. These interactions will modify all components of the coupled system including the Ekman flow itself since the wind stress is going to change.

Fig. 3*A* shows the equatorial currents generated by the model in the control experiment. The NECC flows from west to east (red colors within the black box) against the prevailing easterly trade winds (vectors) over the tropical Pacific. It also depicts the NEC and SEC to the north and south of NECC. A similar

but much weaker eastward current, the South Equatorial Countercurrent (SECC), occurs in the Southern Hemisphere. The SECC does not extend beyond the western Pacific.

The effect of the imposed perturbations is shown in detail in Fig. 3 *B*–*E*. At first, we focus on the 0.1*Vis experiment. As expected, the zonal surface velocity along the NECC is reduced (Fig. 3 *B* and *D*), which is consistent with the strengthening of the westward Ekman velocity. The NEC also weakens which can be explained by changes in the wind forcing. Specifically, there develops an anomalous divergence of wind stress around the NECC, forcing a southwesterly wind stress anomaly over the NEC and strengthening this current. The SEC, flowing on both sides of the equator, is also affected as the southward wind stress anomaly induces westward Ekman velocity in the northern hemisphere but eastward anomaly in the southern hemisphere.

Because the NECC transports warm water from the western Pacific warm pool to the colder eastern Pacific, its changes induce SST and precipitation anomalies in the central and eastern Pacific (Fig. 4 *C* and *D*). In the 0.1*Vis experiment we observe a clear cooling along the NECC path in eastern and central Pacific. This can be attributed to the reduced transport of warm water by the NECC as evident from a decrease of the SST advection term in the temperature equation in the steady state (*SI Appendix*, Fig. S2*D*). The time evolution of key variables in *SI Appendix*, Fig. S3 shows rapid changes of NECC velocity after the imposed viscosity modification, followed by changes in SST and precipitation, which demonstrates that the weakening of the countercurrent is the cause of SST cooling in the eastern Pacific north of the equator. Subsequently, the surface cooling reduces local convection, causing high atmospheric pressure and wind divergence anomalies near the surface, as well as reduced precipitation, indicative of ITCZ weakening. Atmospheric response to the cooling generally follows the Matsuno-Gill model (20–22).

We have already noted the anomalous wind divergence in Fig. 3*D* which explains the induced changes in the NEC and SEC. The generation of those anomalous winds appears to trigger the wind-evaporation-SST (WES) feedback (19, 23). Specifically, the weakening of southeasterly trade winds reduces evaporation and warms SST to the south of the equator, while the resultant anomalous SST gradient across the equator amplifies the trade wind weakening (Fig. 4*C*).

When we increase viscosity in the 10*Vis experiment, we observe generally opposite changes in the equatorial mean state, including a stronger NECC (Fig. 3 *C* and *E*), warmer SSTs in the central and eastern Pacific along the NECC path, higher precipitation, a stronger ITCZ, and stronger wind convergence (Fig. 4*D*).

Fig. 5 shows the profiles of the zonal mean SST, precipitation and zonal surface current over the Pacific Ocean for the entire range of perturbation experiments (0.02*Vis, 0.1*Vis, 10*Vis, and 50*Vis). In both experiments with smaller viscosity, the NECC slows down resulting in a colder SST and weaker precipitation. The weakening of the NEC and interhemispheric dipole-like changes of the SEC across the equator can be seen as well (Fig. 5*C*). We also see SST warming and precipitation increase to the north and especially south of the NECC due to the WES feedback. In the 10*Vis and 50*Vis experiments, we observe a stronger NECC with warmer SSTs and higher precipitation along the NECC path.

Changes in the NECC total zonal transport (Fig. 2 *B* and *C*) indicate that the NECC geostrophic component is indeed modified in the perturbation experiments, which is related to

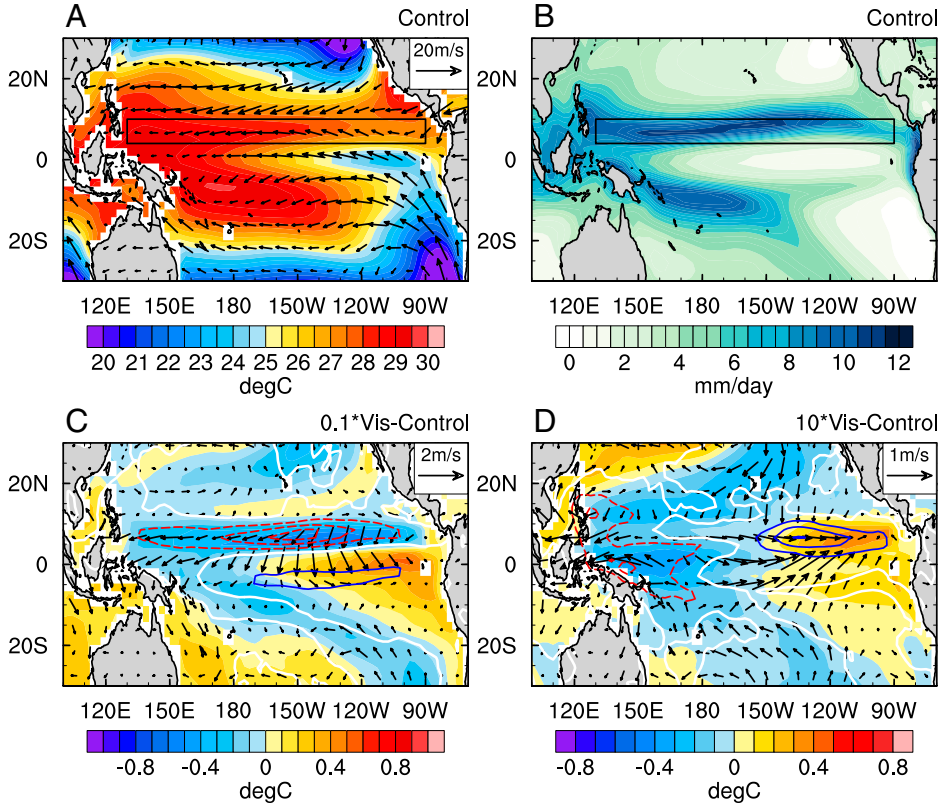

Fig. 4. (*A*) Annual mean SST (colors) and surface wind speed (vectors). (*B*) Annual mean precipitation in the control simulation. (*C* and *D*) SST, wind, and precipitation anomalies relative to the control in the 0.1*Vis and 10*Vis perturbation experiments. Blue, red, and white contours indicate positive, negative, and zero precipitation anomalies with 1 mm/day intervals, respectively. Wind speed is estimated at 925 hPa.

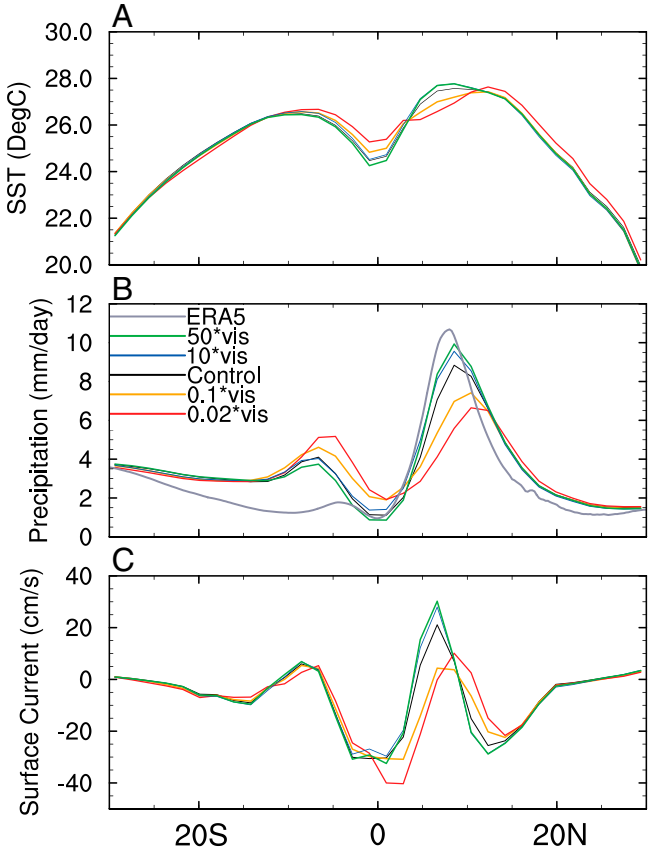

Fig. 5. Zonal mean profiles of (*A*) SST, (*B*) precipitation, and (*C*) zonal surface velocity in the Pacific Ocean for different perturbation experiments and the control simulation. Black, red, orange, dark blue, and green lines indicate the control run, and the 0.02*Vis, 0.1*Vis, 10*Vis, and 50*Vis experiments, respectively. The gray line in (*B*) represents observational data from an observational reanalysis data (ERA5). SST and precipitations are averaged between 150°W–90°W and the ocean zonal surface velocity is averaged between 150°E–150°W. Annual mean profiles are shown.

changes in wind stress divergence/convergence. The annual mean Ekman vertical velocity, calculated from the equation $w = \frac{1}{\rho} curl(\tau/f)$, is shown in *SI Appendix*, Fig. S4*A*.

In the control experiment, positive mean wind stress curl south of the NECC causes the divergence of Ekman transport, lowers sea surface height, and induces Ekman upwelling which raises the isotherms (Fig. 1*B*). In the lower viscosity experiments (0.1*Vis), a weaker ITCZ leads to an anomalous anticyclonic pattern of wind stress, inducing anomalous convergence of Ekman transport. Subsequently, surface water piles up along the northern flank of the NECC, leading to the deepening of the thermocline there and a smaller SSH slope across the NECC (*SI Appendix*, Fig. S4*B*). The SSH changes are shown in *SI Appendix*, Fig. S5*D*, while *SI Appendix*, Fig. S5*A* depicts the annual mean zonal Sverdrup transport in the Pacific Ocean in the control run showing the NECC and NEC.

As already discussed, trade winds converge toward the ITCZ where a local zonal wind minimum develops. This minimum in the easterly wind in the deep tropics and a wind maximum in the subtropics set a region with a positive wind stress curl and a northward pressure gradient force. This pressure gradient force is balanced by the Coriolis force, which implies an eastward countercurrent. Therefore, the increase of sea surface height along the NECC northern flank flattens the SSH gradient across this current, weakening the NECC geostrophic component as well as the NEC (*SI Appendix*, Fig. S5 *B* and *D*). In the low viscosity experiments, the anomalous rise of sea surface height relative to the control simulation weakens both currents. In contrast, in the 10*Vis experiment we see anomalous upwelling, and strengthened NECC and NEC (*SI Appendix*, Figs. S4*C* and S5*E*).

Fig. 6*A* shows the annual mean vertical structure of the zonal currents at 170°W in both control and perturbation experiments. Four upper-ocean currents are prominent: SECC, SEC, NECC, and NEC. The Equatorial Undercurrent (EUC) is located at around 200 m depth and flows eastward. The climatology and anomaly in the 0.1*Vis experiment (Fig. 6 *B* and *D*) indicate that the NECC and NEC are both weakened and there is also a slight poleward shift of the NECC in the reduced viscosity scenario. This poleward shift is related to the poleward shift of the ITCZ as it follows the warmest surface waters (Fig. 5).

Further, the northern part of the SEC strengthens while the southern part weakens, experiencing opposite changes in the two hemispheres. The EUC strengthens, which results from the strengthening of easterly winds along the equator (Fig. 3*D*). In the 10*Vis experiment (Fig. 6 *C* and *E*), we can find a strengthening and a slight equatorward shift of the NECC, opposite to the low viscosity experiments.

These results suggest that the coupled dynamics of the NECC and ITCZ is affected by the WASP feedback. A reduced viscosity along the NECC weakens the near-surface eastward velocity. This reduces the transport of warm water from the west to the east thus decreasing SST in the central and eastern tropical Pacific along the NECC path. Colder SST weakens convection in the east, decreasing surface wind convergence. The weaker convergence reduces wind curl and hence further weakens the NECC. This loop amounts to a positive feedback between the NECC and ITCZ, amplifying the initial changes imposed solely through friction-driven surface Ekman flow. The direction of changes reverses if we increase viscosity as in the 10*Vis experiment, as shown in the flowchart in Fig. 7.

The coupling of the NECC and ITCZ is further illustrated in Fig. 8*A*, which shows monotonic dependence of the ITCZ intensity on the NECC velocity. The latitude of the ITCZ centroid in the northern hemisphere shows a poleward shift in the low viscosity experiments and a slight equatorward shift in the high viscosity experiment (Fig. 8*B*) as discussed before. Changes of the strength of the SPCZ also occur (Fig. 8 *C* and *D*). In fact, we observe a seesaw relationship between the ITCZ and SPCZ: when the ITCZ becomes weaker, the SPCZ becomes stronger and vice versa. In addition, the SPCZ shifts meridionally, albeit slightly, in the same direction as the ITCZ.

The opposite changes in the ITCZ and SPCZ intensities are similar to the seesaw behavior of these two precipitation bands described by Zhao and Fedorov (19). They have demonstrated that in the tropical Pacific the response of the coupled ocean-atmosphere system to a hemispherically asymmetric thermal forcing (surface heat fluxes) involves interhemispheric seesaw changes in tropical precipitation, such that the latitudinal position of these rain bands remains largely fixed but their intensities follow a robust inverse relationship.

Conclusions

In our study, we conducted a suite of experiments wherein we perturbed the NECC by modifying the model vertical eddy viscosity along its path. We find that the resulting, relatively small changes in the surface Ekman velocity within the NECC yield systematic changes in the geostrophic current. These changes reflect a positive feedback (WASP) due to ocean-atmosphere interactions—a

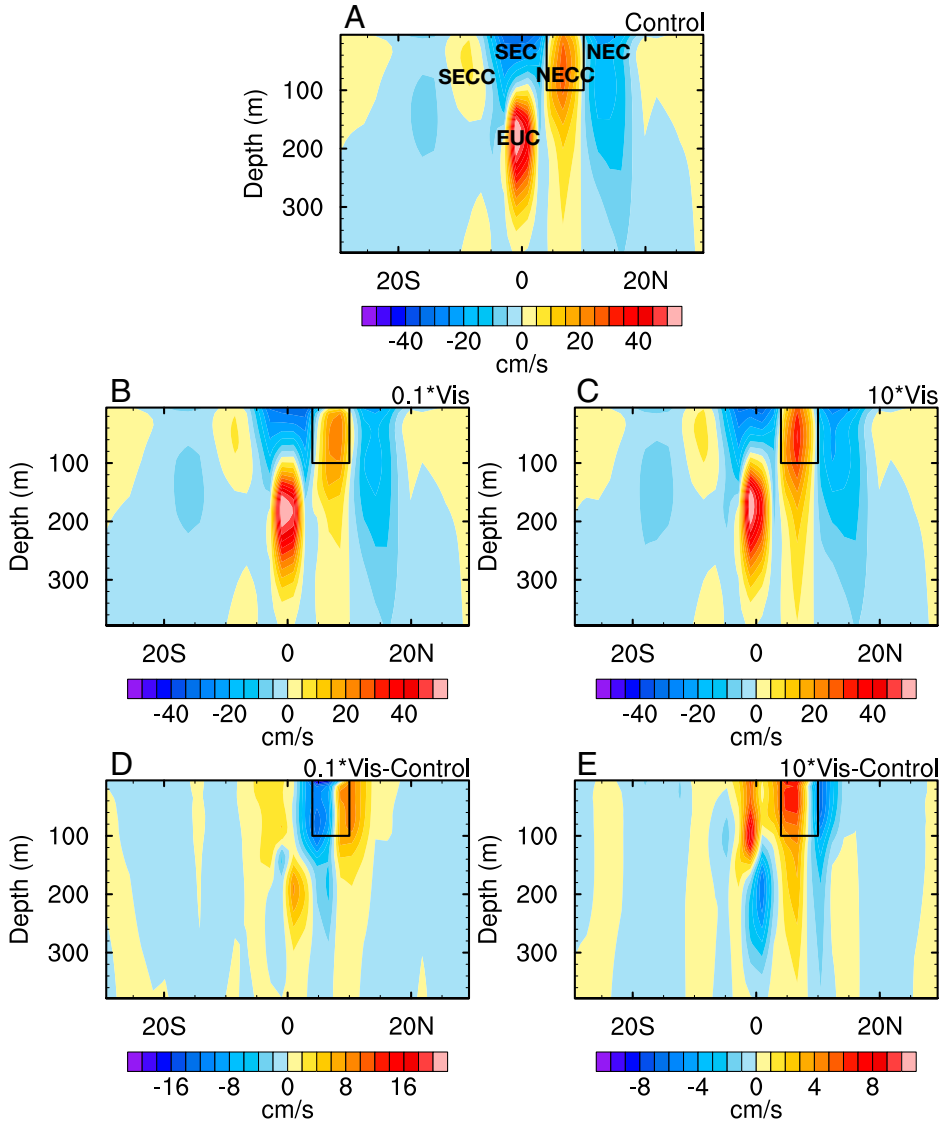

Fig. 6. (*A*–*C*) The vertical structure of the annual mean zonal current at 170°W in the control simulation, and the 0.1*Vis and 10*Vis experiments. (*D* and *E*) Velocity anomalies in the two perturbation experiments relative to the control. The rectangular box marks the area where the model vertical viscosity has been modified.

stronger current leads to greater eastward SST advection and, ultimately, a stronger wind stress curl, reinforcing initial changes.

In fact, most of subsequent changes in the NECC result from changes in wind stress curl and hence sea surface heights, and thus largely depends on changes in geostrophic velocity. Although the wind stress anomalies do modify the surface westward Ekman velocity further, these changes remain relatively small compared to the geostrophic current.

A similar countercurrent occurs under the Atlantic ITCZ, with a qualitatively analogous pattern of winds, so that our conclusions here may also apply to the Atlantic. A further investigation is needed, however, since in the Atlantic the zonal SST gradient is weaker and the meridional structure of the NECC is more complicated.

Both ocean and coupled GCMs commonly simulate a too-weak countercurrent in the Pacific ocean (2, 5, 10, 24, 25). The recent study of Tseng et al. (26) highlights this problem as their ocean GCM multimodel mean composite shows almost no NECC. Models forced with the CORE-II wind stress and surface fluxes, which presumably provide a close approximation to the observed surface momentum and heat fluxes, still have difficulties in reproducing the NECC, both its strength and meridional structure (25). Coupled GCMs have similar problems, which may be related in part to insufficient model resolution and deficiencies in the generated wind stress (10), but unresolved physics and/or inadequate representation of ocean-atmosphere interactions could be another important issue.

From an atmospheric perspective the position and the intensity of the ITCZ is generally set by the SST distribution in the tropics. A too-weak WASP feedback results in a weak NECC, colder SSTs along its path, and hence a weak ITCZ, which can contribute to the double-ITCZ problem persistent in climate models as discussed in the introduction (15, 17, 27), as a weaker ITCZ in the northern hemisphere tends to favor a stronger secondary convergence zone in the southern hemisphere (Fig. 5 and *SI Appendix*, Fig. S6; 19).

Indeed, Fig. 5*B* depicts precipitation data showing a stronger ITCZ and a weaker SPCZ in the observations (gray line) than in the control simulation, which is indicative of the model double-ITCZ problem. Our experiments with enhanced vertical viscosity and hence stronger NECC strengthen the ITCZ and weaken the SPCZ, reducing this precipitation bias relative to the control by approximately 10%. As the NECC remains weaker than the observations, the problem does not disappear

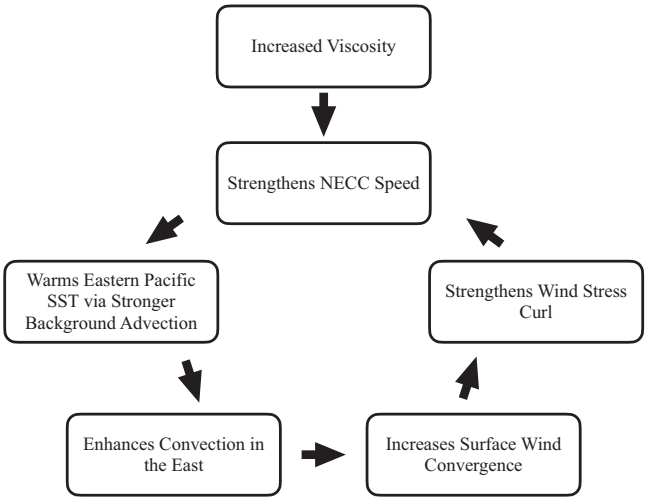

Fig. 7. A flowchart illustrating the positive WASP feedback loop triggered by an increase in vertical viscosity. Note that when we change viscosity initially, this modifies Ekman (near-surface) flow. The subsequent ocean–atmosphere interactions predominantly affect the geostrophic current.

completely. In the experiments with a weak NECC, the ITCZ weakens while the SPCZ strengthens, which amplifies the double-ITCZ problem. Consequently, between the lowest and highest viscosity cases (weak and strong NECC) the precipitation bias is reduced by nearly 40%.

Ultimately, these results sheds light on the coupled dynamics of the NECC and ITCZ, which involves a comprehensible set of processes as illustrated in Fig. 7 and is critical for climate model simulations. Our work demonstrates the complexity and often unforeseen consequences of this ocean-atmosphere coupling for the tropical region.

Methods

Experiment Approach. Theoretically, the NECC can be decomposed into geostrophic and Ekman components. The latter component is directly forced by wind stress through friction. The eastward geostrophic current is associated with wind stress curl and the corresponding deformation of SSH. The meridional pressure gradient due to SSH is compensated at depth by the pressure gradient due to the south-north isotherm slope. Our approach is to force changes in the Ekman component of the NECC by modifying the model's vertical eddy viscosity and then analyze the resulting changes in this current and the entire NECC/ITCZ complex caused by ocean-atmosphere interaction.

Assuming for simplicity that the winds in the region are predominantly zonal, which is a good approximation in the western and central part of the basin, one can calculate the surface zonal and meridional Ekman velocities away from the equator as

$$u_{Ek} = v_{Ek} = \frac{\tau}{\rho\sqrt{2f\nu}}, \quad [1]$$

where τ is zonal wind stress, ρ is the density of seawater, f is the Coriolis parameter, and ν is vertical eddy viscosity in the upper ocean used in the momentum equations (28). In the Northern Hemisphere, the direction of the surface Ekman velocity is 45° to the right of the direction of wind stress. Therefore, easterly trade winds generate a

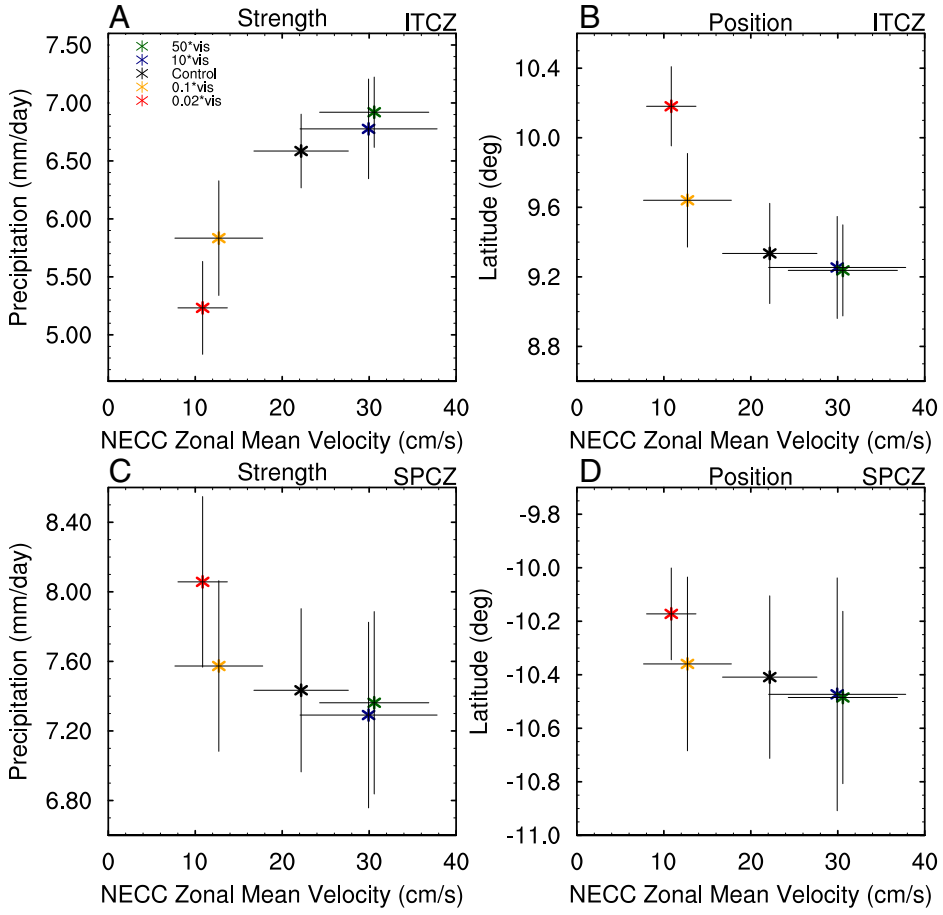

Fig. 8. (*A*) The strength and (*B*) position of the ITCZ in the Pacific Ocean versus the NECC maximum zonal mean velocity; and (*C* and *D*) the same for the SPCZ. Different colors represent different experiments. The asterisks and gray bars indicate average values and one SD for each experiment. The ITCZ and SPCZ intensities are defined as the annual mean precipitation averaged over 5°N–15°N, 150°E–90°W, 5°S–15°S, and 150°E–150°W, respectively. The latitude is defined as the centroid of the precipitation in the respective hemisphere. See *Materials and Methods* for how the NECC maximum zonal mean velocity is defined.

westward zonal component in the surface Ekman velocity. Based on this expression, we can alter the surface Ekman component of the NECC by modifying viscosity v. For example, increasing viscosity would reduce the westward surface Ekman current thus leading to a stronger surface flow in the NECC.

Unlike the surface Ekman velocity, depth-integrated Ekman transport, computed for zonal wind stress as

$$U_{Ek} = 0;\ V_{Ek} = \tau/f, \quad [2]$$

is independent of viscosity and directed strictly northward. Consequently, in the absence of coupled ocean-atmosphere feedbacks, by modifying viscosity we would be able to change only the NECC surface flow, but not its total zonal transport. However, in the presence of positive feedbacks affecting surface wind stress, one can expect further changes in the NECC, including changes in its geostrophic velocity and total zonal transport.

It is important that the Ekman layer depth remains deeper than the ocean mixed layer depth in the NECC region (20–30 m) throughout most of our experiments (except for 0.02*Vis); consequently, changes in the surface Ekman velocity can modulate the transport of warm surface water from west to east and hence alter SST.

In addition to Ekman theory, to analyze the results, we also use a theoretical expression for the depth-integrated volume transport of the geostrophic flow. It is obtained by integrating the meridional Sverdrup transport (28, 29) with the use of the continuity equation:

$$U_{sverdrup} = \frac{1}{\beta}\int_{x}^{x_e} \frac{\partial(curl\ \boldsymbol{\tau})}{\partial y}\, dx, \quad [3]$$

where $U_{sverdrup}$ is depth-integrated zonal velocity (or zonal transport), x and y are the horizontal coordinates corresponding to longitude and latitude, x_e is the eastern boundary of the Pacific basin, and β is the planetary vorticity gradient in the NECC region ($\beta = df/dy$). This relationship is valid in the ocean interior. Critically, zonal flow given by this expression depends on an integral of wind stress curl.

GCM Perturbation Experiments. We employ the NCAR Community Earth System Model (CESM1.2), a fully coupled model broadly used for climate projection and sensitivity studies (30, 31). The model's main components are Community Atmosphere Model-5.3 and Parallel Ocean Program POP2. We run the model at the horizontal resolution of f19_gx1v6: 1.9° × 2.5° for the atmosphere and land components, and approximately 1° for the ocean and ice components. The grid for the ocean component becomes finer approaching the equator and the latitudinal resolution reaches approximately 0.3°.

We conduct one control experiment and four perturbation experiments with modified viscosity. In the control experiment the NECC reaches the maximum speed of 23 cm/s (Fig. 2*A*), which is approximately half of the observed value. At 170°W, its simulated total zonal transport reaches nearly 17Sv (Fig. 2*B*), which is in the ballpark of the observations, even though the available observational values depend strongly on the analysis, time period, and longitude (4–6, 8, 26, 32, 33).

In the perturbation experiments, to alter the NECC, we modify the model vertical eddy viscosity within an upper-ocean band along the NECC path (4°N–10°N, 130°E–90°W, 0–100 m). To change viscosity, we simply multiply the vertical viscosity coefficient computed by the model in this band by factors of 50, 10, 0.1, and 0.02, respectively. We refer to these coefficients as viscosity multipliers (VM) and call the experiments as 50*Vis, 10*Vis, 0.1*Vis, and 0.02*Vis.

We stress however that the actual range of the imposed viscosity changes is much smaller than the VM range, as evident from *SI Appendix*, Fig. S7 that shows vertical viscosity used in the momentum equation ("output viscosity"). In fact, average viscosity within the NECC region varies from approximately 60 cm^2/s in the 0.02*Vis experiment to 200 cm^2/s in the control run and to 2,000 cm^2/s in the 50*Vis experiment. This smaller range can be explained by a negative feedback related to the dependence of model viscosity on the Richardson number as the latter depends on the vertical shear of the flow which in turn is affected by viscosity. Increasing viscosity reduces the shear, which acts to decrease viscosity.

We also note that no spurious gradients or shears arise along the edges of the box with viscosity perturbation, since any strong gradients are quickly relaxed by the adjustment of the currents. The aforementioned negative feedback also plays a role by reducing the imposed viscosity contrasts.

Each experiment continues for 100 y and the last 50 y are used for analysis after the climate reaches a new equilibrium. When showing the spatial structure of anomalies in the perturbation experiments, we focus on the 0.1*Vis and 10*Vis experiments since the 0.02*Vis and 50*Vis simulations, respectively, produce qualitatively similar patterns.

In addition to modifying vertical viscosity, we have considered other approaches to alter the NECC intensity, such as changing the wind stress meridional profile or ocean thermal structure. However, these methods are either too complicated to implement, or they are not physically consistent within the coupled ocean-atmosphere system, or have additional major impacts on the tropical climate.

Finally, the NECC maximum zonal mean velocity is estimated by zonally averaging monthly surface velocity between 150°E–120°W (i.e., where the model countercurrent is almost uniform zonally), then taking the maximum value between 4°N–10°N, and then computing its annual-mean value. For brevity, it is referred to as the NECC zonal mean velocity in Figs. 2 and 8.

Data Availability. Data have been deposited in coupled dynamics of the North Equatorial Countercurrent and the Intertropical Convergence Zone (https://doi.org/10.5061/dryad.3r2280ghg) (34).

ACKNOWLEDGMENTS. This study has been supported by the National Aeronautics and Space Administration (80NSSC21K0558) and the National Oceanic and Atmospheric Administration (NA20OAR4310377). Additional support is provided by the ARCHANGE project (ANR-18-MPGA-0001, France). We thank Billy Kessler and Kris Karnauskas for reviewing the manuscript, and the editor for helpful suggestions. We also thank the editor of the paper, Kerry Emanuel, for critical suggestions in improving the paper.

1. K. Wyrtki, R. Kendall, Transports of the pacific equatorial countercurrent. *J. Geophys. Res.* **72**, 2073–2076 (1967).
2. S. Philander, W. Hurlin, A. Seigel, Simulation of the seasonal cycle of the tropical pacific ocean. *J. Phys. Oceanogr.* **17**, 1986–2002 (1987).
3. G. Reverdin, C. Frankignoul, E. Kestenare, M. J. McPhaden, Seasonal variability in the surface currents of the equatorial pacific. *J. Geophys. Res. Oceans* **99**, 20323–20344 (1994).
4. J. R. Donguy, G. Meyers, Mean annual variation of transport of major currents in the tropical pacific ocean. *Deep Sea Res. Part I Oceanogr. Res. Pap.* **43**, 1105–1122 (1996).
5. Z. Yu, J. P. McCreary Jr., W. S. Kessler, K. A. Kelly, Influence of equatorial dynamics on the pacific north equatorial countercurrent. *J. Phys. Oceanogr.* **30**, 3179–3190 (2000).
6. W. S. Kessler, The circulation of the eastern tropical pacific: A review. *Prog. Oceanogr.* **69**, 181–217 (2006).
7. Y. C. Hsin, B. Qiu, Seasonal fluctuations of the surface North Equatorial Countercurrent (NECC) across the Pacific basin. *J. Geophys. Res. Ocean.* **117**, C06001 (2012).
8. G. C. Johnson, B. M. Sloyan, W. S. Kessler, K. E. McTaggart, Direct measurements of upper ocean currents and water properties across the tropical pacific during the 1990s. *Prog. Oceanogr.* **52**, 31–61 (2002).
9. D. Urbano, M. Jochum, I. Da Silveira, Rediscovering the second core of the Atlantic NECC. *Ocean Model.* **12**, 1–15 (2006).
10. J. N. Brown, A. V. Fedorov, Mean energy balance in the tropical Pacific Ocean. *J. Mar. Res.* **66**, 1–23 (2008).
11. T. Schneider, T. Bischoff, G. H. Haug, Migrations and dynamics of the intertropical convergence zone. *Nature* **513**, 45–53 (2014).
12. T. Lee, D. E. Waliser, J. L. F. Li, F. W. Landerer, M. M. Gierach, Evaluation of CMIP3 and CMIP5 wind stress climatology using satellite measurements and atmospheric reanalysis products. *J. Clim.* **26**, 5810–5826 (2013).
13. K. J. Richards, S. P. Xie, T. Miyama, Vertical mixing in the ocean and its impact on the coupled ocean–atmosphere system in the eastern tropical pacific. *J. Clim.* **22**, 3703–3719 (2009).
14. H. Masunaga, T. S. L'Ecuyer, Equatorial asymmetry of the east Pacific ITCZ: Observational constraints on the underlying processes. *J. Clim.* **24**, 1784–1800 (2011).
15. J. L. Lin, The double-ITCZ problem in IPCC ar4 coupled GCMs: Ocean–atmosphere feedback analysis. *J. Clim.* **20**, 4497–4525 (2007).
16. Y. T. Hwang, D. M. Frierson, Link between the double-intertropical convergence zone problem and cloud biases over the Southern Ocean. *Proc. Natl. Acad. Sci. U.S.A.* **110**, 4935–4940 (2013).
17. G. Li, S. P. Xie, Tropical biases in CMIP5 multimodel ensemble: The excessive equatorial pacific cold tongue and double ITCZ problems. *J. Clim.* **27**, 1765–1780 (2014).
18. G. J. Zhang, X. Song, Y. Wang, The double ITCZ syndrome in GCMs: A coupled feedback problem among convection, clouds, atmospheric and ocean circulations. *Atmospheric Res.* **229**, 255–403 (2019).
19. B. Zhao, A. Fedorov, The seesaw response of the intertropical and South Pacific convergence zones to hemispherically asymmetric thermal forcing. *Clim. Dyn.* **54**, 1639–1653 (2020).
20. T. Matsuno, Quasi-geostrophic motions in the equatorial area. *Kisho Shushi. Dai2shu* **44**, 25–43 (1966).
21. A. E. Gill, Some simple solutions for heat-induced tropical circulation. *Q. J. R. Meteorol. Soc.* **106**, 447–462 (1980).
22. R. S. Lindzen, S. Nigam, On the role of sea surface temperature gradients in forcing low-level winds and convergence in the tropics. *J. Atmos. Sci.* **44**, 2418–2436 (1987).
23. S. P. Xie, S. G. H. Philander, A coupled ocean-atmosphere model of relevance to the ITCZ in the eastern Pacific. *Tellus, Ser. A, Dyn. Meterol. Oceanogr.* **46**, 340–350 (1994).

24. N. Grima *et al.*, Sensitivity of an oceanic general circulation model forced by satellite wind stress fields. *J. Geophys. Res. Oceans* **104**, 7967–7989 (1999).
25. G. Danabasoglu *et al.*, North Atlantic simulations in coordinated ocean-ice reference experiments phase ii (core-ii). Part i: Mean states. *Ocean Model.* **73**, 76–107 (2014).
26. Yh. Tseng *et al.*, North and equatorial Pacific Ocean circulation in the core-ii hindcast simulations. *Ocean Model.* **104**, 143–170 (2016).
27. N. J. Burls, L. Muir, E. M. Vincent, A. Fedorov, Extra-tropical origin of equatorial Pacific cold bias in climate models with links to cloud albedo. *Clim. Dyn.* **49**, 2093–2113 (2017).
28. R. H. Stewart, *Introduction to Physical Oceanography* (Texas A&M University, 2008).
29. H. U. Sverdrup, Wind-driven currents in a baroclinic ocean; with application to the equatorial currents of the eastern Pacific. *Proc. Natl. Acad. Sci. U.S.A.* **33**, 318–326 (1947).
30. N. J. Burls, A. V. Fedorov, Wetter subtropics in a warmer world: Contrasting past and future hydrological cycles. *Proc. Natl. Acad. Sci. U.S.A.* **114**, 12888–12893 (2017).
31. S. Hu, A. V. Fedorov, Cross-equatorial winds control el niño diversity and change. *Nat. Clim. Chang.* **8**, 798–802 (2018).
32. K. Wyrtki, B. Kilonsky, Mean water and current structure during the Hawaii-to-Tahiti shuttle experiment. *J. Phys. Oceanogr.* **14**, 242–254 (1984).
33. B. A. Taft, W. S. Kessler, Variations of zonal currents in the central tropical pacific during 1970 to 1987: Sea level and dynamic height measurements. *J. Geophys. Res. Oceans* **96**, 12599–12618 (1991).
34. Z. Li, A. V. Fedorov, Data from "Coupled dynamics of the North Equatorial Countercurrent and Intertropical Convergence Zone with relevance to the double-ITCZ problem." Dryad. https://doi.org/10.5061/dryad.3r2280ghg. Deposited 5 July 2022.